2026 IEEE International Conference on Robotics and Automation (ICRA 2026)
June 1-5, 2026. Vienna, Austria

A Tri-axial FBG-based Force Sensor at the Tool Tip of a Continuum Manipulator for Single-Port Access Surgery

Jiading Zhang[1], Lijun Hao[1], Siqi Liu[1], Jiangran Zhao[2], Jiamiao Gong[3], Kai Xu[4], Sheng Liu[3], Zhe Zheng[3], and Tangwen Yang[1]

***Abstract*— The absence of force feedback remains a major bottleneck in the development of robotic laparoendoscopic single-site (R-LESS) surgery, reducing the control precision of surgical instruments and increasing the risk of tissue damage. To address this challenge, we propose a miniature triaxial force sensor based on Fiber Bragg Grating (FBG), featuring high precision, nonlinear decoupling capability, and seamless integration with the tool tip of a continuum manipulator for single-port access surgery. The sensor features a monolithic elastic body with a dumbbell-shaped groove, where four FBGs are symmetrically arranged at 90° intervals around the circumference to form a redundant measurement unit, thereby enhancing sensing accuracy. A novel Whale Migration Algorithm Based Kernel Extreme Learning Machine (WMA-KELM) is introduced to address the nonlinear coupling influences arising from manipulator integration, demonstrating superior accuracy and robustness compared to conventional methods. Experimental results show that within the ranges of axial force [0 N, 5 N] and radial force [-2.5 N, 2.5 N], the maximum full-scale (FS) error is less than 1% in all dimensions, the maximum RMSE is 0.0308 N, and the maximum repeatability error is within ±0.24%. These results validate the force sensor integrated with the continuum manipulator, and the proposed algorithm is effective and reliable.**

I. INTRODUCTION

With the advancement of minimally invasive surgical techniques, robotic laparoendoscopic single-site (R-LESS), which integrates with robotic arms and high-definition imaging systems, has emerged in a master-slave control mode and reshaped the operational paradigm for complex surgical procedures[1], [2]. These systems typically deploy specialized laparoscopic instruments and endoscopic cameras through a single miniature incision (2–3 cm), enabling accessible diagnostics or intricate therapeutic interventions within the abdominal, thoracic, or pelvic cavities[3]. These systems successfully address the limitations in open surgery, such as low precision and dexterity, unclear visualization, and high surgeon fatigue[4], [5]. R-LESS has rapidly evolved and gained incremental clinical adoption. However, the absence of force feedback remains a critical challenge in R-LESS surgery. The statistical analysis of surgical trainees' procedures revealed that excessive or insufficient force accounted for approximately 56% of surgical errors in laparoscopic cholecystectomies, because the forces perceived at the tool–tissue interface are often amplified or distorted due to internal friction within instruments and lever-induced force amplification from surrounding tissues and organs[6], [7]. The force feedback, delivered through physical tactile sensations or auditory/visual cues, improves surgical accuracy and operational efficiency in R-LESS surgery, while simultaneously facilitating skill acquisition and shortening the learning curve for novice surgeons[8], [9]. Accurate and robust force sensing technology is pivotal for enabling such feedback[10], [11]. Therefore, this paper aims to develop a miniaturized, high-precision, and reliable triaxial force sensor specifically designed for the tool tip of a continuum manipulator for single-port access surgery.

Piezoresistive force sensors have received significant attention due to stability and sensitivity, but require complex structural design and precise installation to achieve optimal performance[8]. Capacitive force sensors effectively eliminate hysteresis effects, maintaining high sensitivity and stability even under varying temperature conditions[12]. However, they are constrained by the interference from parasitic capacitance[13]. Piezoelectric force sensors are able to measure dynamic forces through the piezoelectric effect, but they cannot measure static forces and are susceptible to external electromagnetic interference[14]. A notable emerging trend is to integrate fiber Bragg grating (FBG) force sensors into surgical robots or instruments, enabling real-time measurement of interactive forces between surgical instruments and tissues, while offering the advantages over other force-sensing technologies such as higher accuracy, inherent biocompatibility, and compatible electromagnetic interference[15], [16]. Gao et al.[17] and Ping et al.[18] devised triaxial FBG force sensors which are capable of measuring forces along arbitrary directions in gastric endoscopy and catheter ablation, but the influence of temperature variations has not been examined. Li et al.[19] developed a high-precision triaxial FBG force sensor with temperature compensation and fault-tolerant strategies, enabling accurate and reliable three-dimensional force measurement even under sensor failure. However, the photocurable resin housing has relatively low mechanical strength, which deteriorates its performance under high loads. Gan et al. [20] proposed a

This work is supported by the National Key Research and Development Program of China under Grant 2022YFB4700902. (Corresponding author: Tangwen Yang).

[1]Jiading Zhang, Lijun Hao, Siqi Liu, and Tangwen Yang are with the School of Computer and Information Technology, Beijing Jiaotong University, Beijing 100044, China. twyang@bjtu.edu.cn

[2]Jiangran Zhao is with Beijing Surgerii Robotics Company Limited, Beijing 100192, China. jiangran.zhao@surgerii.com

[3]Jiamiao Gong, Sheng Liu, and Zhe Zheng are with the National Center for Cardiovascular Disease, Fuwai Hospital, Chinese Academy of Medical Sciences, Beijing 100037, China.

[4]Kai Xu is with the School of Mechanical Engineering, Shanghai Jiao Tong University, Shanghai 200240, China. k.xu@sjtu.edu.cn

TABLE I

SENSOR DESIGN REQUIREMENTS

Characteristics	Specifications
Dimension	Sensor Diameter $= 6.0$ mm
Force range	$0 \text{ N} \leq F_z \leq 5.0 \text{ N}; \quad \lvert F_x \rvert, \lvert F_y \rvert \leq 2.5 \text{ N}$
Precision	1.0% FS
Repeatability	$\pm 0.5\%$ FS

miniature triaxial FBG force–temperature sensor for catheter ablation, featuring independent temperature sensing and nonlinear neural network-based force measurement, demonstrating high sensitivity and accuracy. However, the sensor does not fully cover the temperature range, and limits its applicability under certain thermal conditions. In our previous work, we designed a miniature triaxial force sensor integrated at the tip of a flexible ureteroscope [21], and developed a morphological wavelet-based method to extract force signals from surgical instruments [22]. However, the differences in size and functional requirements in the continuum manipulator make it incapable for single-port access surgery.

Sensor accuracy can be affected by many factors including structural design, machining precision, fiber optic splicing, and internal stresses. Nonlinear coupling error is inevitable and thus requires the decoupling of output signals[23]. Gao et al.[17] proposed a structure of parallel and series flexible hinges for self-decoupling in multi-axis sensors. However, this structure causes assembly complicated and introduces FBG at the sensor center, which is detrimental to system integration. The least squares (LS) approach is widely used for sensor signal decoupling, yet it is sensitive to ill-conditioned matrices, which may undermine the reliability of the decoupling results[24]. Oh et al. [25] introduced a decoupling framework based on deep neural networks (DNNs), and compares its performance with traditional LS-based methods and single-hidden-layer networks. Although their approach achieved a maximum error of 12.91% on Full-Scale(FS), the high computation load associated with the complex network limits its application in real-time scenarios. Li et al.[19] made a comparison of LS, Back Propagation Neural Networks (BPNN), and Extreme Learning Machines (ELM). Results demonstrated that ELM exhibited significant advantages, and its maximum mean squared error (MSE) is less than 0.77 mN during training. However, ELM is relatively sensitive to initial parameters.

This paper introduces a miniaturized triaxial FBG force sensor at the tool tip of a continuum manipulator used in single-port access surgery. The hollow nickel-titanium alloy structure with dumbbell-shaped grooves enhances its sensitivity while allowing seamless integration with the continuum manipulator. A nonlinear decoupling method is proposed based on the Whale Migration Algorithm Based Kernel Extreme Learning Machine (WMA-KELM), which demonstrates superior performance in both accuracy and prediction time. The sensor has been integrated into the continuum manipulator, and experiments verify its effectiveness and reliability.

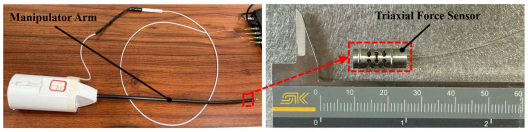

Fig. 1: The continuum manipulator arm (a) and the triaxial force sensor (b).

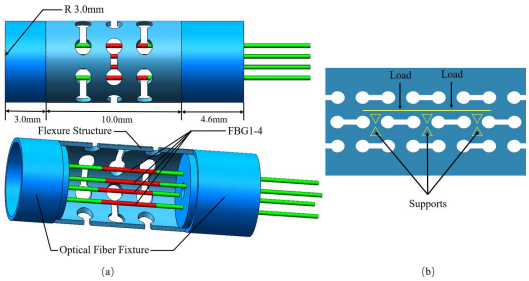

Fig. 2: The schematic of the triaxial force sensor. (a) the force sensing elastomer; (b) the dumbbell-shaped grooves.

II. TRIAXIAL FORCE SENSOR DEVELOPMENT

A. Sensor Design and Fabrication

A single-port surgery robot system typically employs a single channel, through which the manipulator arm is inserted into the body via a single-port trocar [26]. The system features three flexible manipulator arms and a vision arm, enabling tissue retraction, dissection, and high-definition imaging [27]. The force sensor is attached to the end of a surgical instrument, with its drive wires routed through the central channel of the sensor, as shown in Fig. 1, to measure the interactive force between the instrument and soft tissue. The design requirements of the force sensor, as given in Table I, are primarily dictated by the flexibility and dimensional constraints of the manipulator arm, in addition to the force ranges. The diameter of the force sensor is same as the manipulator arm. The maximum axial force F_z is set at 5 N, while the radial forces F_x and F_y are limited to the range -2.5 N to 2.5 N. They are given based on the clinical patient data [28], [29]. The force accuracy and repeatability must be controlled within $\pm 1.0\%$FS and $\pm 0.5\%$FS. Besides, as a medical device, the force sensor must also meet the requirements of biocompatibility, electromagnetic compatibility, and sterilization.

Figure 2 shows the miniature triaxial force sensor integrated into the continuum manipulator. It consists of a hollow cylindrical nickel-titanium elastomer with dumbbell-shaped grooves to balance axial and radial stiffness. Four optical fibers, each etched with a single FBG (Beijing Dijing Optoelectronic Technology Co., Ltd., reflectivity $\geq 85\%$), are arranged at 90° intervals around the neutral axis and fixed within two optical fiber fixtures. The fixtures contain a central through-hole for the instrument drive cable and four peripheral holes for the fibers, ensuring the FBGs are suspended at the elastomer center without encapsulation. Both of the fiber ends are secured with Loctite 4013 adhesive.

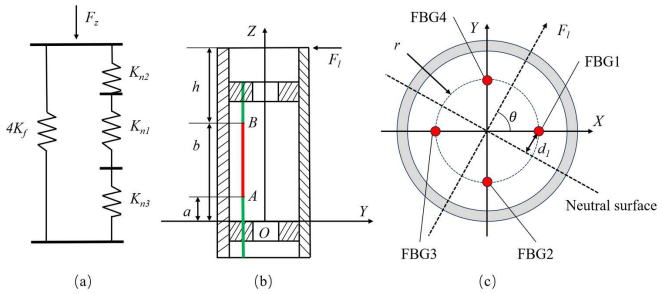

Fig. 3: The equivalent models of the force sensor. (a) the spring model in the axial direction; (b) the cantilever beam model in the radial direction; (c) a cross section.

B. Sensing Principle

When the interactive force acts on the distal instrument, it is transmitted to the sensor, causing the deformation in the section of dumbbell-shaped grooves. As shown in Fig. 3, a Cartesian coordinate system is first established at the center of the fixed end of the flexture structure. The Z-axis is along the centerline of the sensor, and the X- and Y-axes are perpendicular to the Z-axis and are established in complicance with the right-hand convention. Under axial loading, Fig. 3 shows the equivalent spring model of the sensor, and the overall axial stiffness K_z of the sensor, formed by these components in series, can be computed by

$$K_z = \frac{4K_f \cdot (K_{a1} + K_{a2} + K_{a3})}{4K_f + K_{a1} + K_{a2} + K_{a3}} \tag{1}$$

where K_{a1} is the stiffness of the dumbbell-shaped hollow cross-section in the flexture structure, K_{a2} and K_{a3} are respectively the stiffness of the upper and lower portions of the sensor, and K_f is the stiffness of one FBG.

Subsequently, under axial load, the strain on the ith FBG $(i = 1, 2, 3, 4)$ can be given by

$$\varepsilon_{z1} = \varepsilon_{z2} = \varepsilon_{z3} = \varepsilon_{z4} = \frac{F_z}{K_z(b-a)} \tag{2}$$

where F_z is the axial load applied to the sensor, a and b are the distances from the proximal and distal ends of FBG to the origin of the Z-axis, as shown in Fig. 3(b).

As shown in Fig. 3(b), when a radial load is applied to the sensor, the strain on FBG can be computed based on an equivalent cantilever beam, yielding

$$\varepsilon_{ri} = \frac{F_l d_i}{b-a} \int_a^b \frac{h+x}{EI(x) + E_f I_f} dx \tag{3}$$

where ε_{ri} is the strain on the ith FBG $i(i = 1, 2, 3, 4)$ as the radial load F_l is applied, and b_i denotes the distance of each FBG to the force-neutral plane, as shown in Fig. 3(c). E and E_f denote the elastic moduli of the structure material and the optical fiber. $I(x)$ and I_f are their moments of inertia, and h is the length from of the optical fiber end to the load surface.

The force sensor is grooved with hollow sections, allowing it to be modeled equivalently with two cylinders of different radii. Hence, its bending stiffness can be given by a piecewise function:

$$EI(x) = \begin{cases} \dfrac{\pi\left(D_1^4 - d_1^4\right)}{64}, & x \in [a, b] \\ \dfrac{\pi\left(D_2^4 - d_2^4\right)}{64}, & x \in [0, a) \cup (b, b+h] \end{cases} \tag{4}$$

Where D_1 and d_1 are the equivalent outer and inner diameters of the hollowed-out region, D_2 and d_2 are the outer and inner diameters of the sensor.

When the applied radial load is parallel to the positive direction of X axis, FBG2 and FBG4 are on the neutral plane of the force, and $d_2 = d_4 \approx 0$. Meanwhile, FBG1 is compressed and FBG3 is stretched, and $d_1 = d_3 \approx r$. r is the radial distance of FBG to the sensor centerline. Then we have

$$\begin{cases} \varepsilon_{r3} = -\varepsilon_{r1} = \frac{F_l r}{b-a} \int_a^b \frac{h+x}{EI(x)+E_f I_f} dx \\ \varepsilon_{r2} = \varepsilon_{r4} \approx 0 \end{cases} \tag{5}$$

Similarly, due to the symmetrical structure of the sensor, when the radial load is along the positive direction of Y axis, the following equation can be derived:

$$\begin{cases} \varepsilon_{r2} = -\varepsilon_{r4} = \frac{F_l r}{b-a} \int_a^b \frac{h+x}{EI(x)+E_f I_f} dx \\ \varepsilon_{r1} = \varepsilon_{r3} \approx 0 \end{cases} \tag{6}$$

In terms of (2), (5) and (6), the relationship between axial/radial forces and the FBG wavelength drift is given by

$$\begin{bmatrix} \Delta_1 \\ \Delta_2 \\ \Delta_3 \\ \Delta_4 \end{bmatrix} = \frac{\lambda_B(1-p_e)}{b-a} \mathbf{S} \begin{bmatrix} F_x \\ F_y \\ F_z \end{bmatrix} \tag{7}$$

Where $\Delta_i (i = 1, 2, 3, 4)$ denotes the wavelength drift of FBG, λ_B represents the initial wavelength of FBG, p_e represents the effective photo-elastic coefficient. F_x, F_y and F_z are the forces in the three axial directions. $\mathbf{S}$ is given by

$$\mathbf{S} = \begin{bmatrix} -r\int_a^b \frac{h+x}{EI(x)+E_f I_f} dx & 0 & \frac{1}{K_{az}} \\ 0 & r\int_a^b \frac{h+x}{EI(x)+E_f I_f} dx & \frac{1}{K_{az}} \\ r\int_a^b \frac{h+x}{EI(x)+E_f I_f} dx & 0 & \frac{1}{K_{az}} \\ 0 & -r\int_a^b \frac{h+x}{EI(x)+E_f I_f} dx & \frac{1}{K_{az}} \end{bmatrix} \tag{8}$$

TABLE II

PHYSICAL PARAMETERS OF SENSOR COMPONENTS

Parts	Material	Young's modulus (GPa)	Poisson ratio	Density (kg/m^3)
Elastomer	Nickel-titanium alloy	75	0.33	6450
Optical fiber	Silica	72	0.17	2500
Glue	Epoxy resin	3.3	0.33	1180

C. Finite Element Simulations

To design a force sensor that meets the requirements of measurement range and sensitivity, the finite element analysis (FEA) has been done with the Ansys Workbench tool (ANSYS Inc., Pennsylvania). To this end, we design various

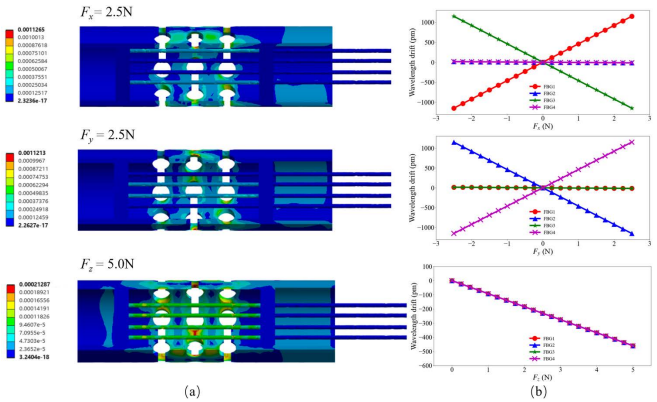

Fig. 4: The FEA results of the force sensor under axial and radial forces. (a) the strain profiles; (b) The wavelength drifts of FBGs.

grooves and adjust their structural parameters to decouple the axial and radial forces on the sensor. The parallel dumbbell-shaped grooves are used in this study because they are able to ensure the structural stability while preserving the stiffness symmetry in the radial direction. The force sensing elastomer consists of three layers, and each layer has four dumbbell-shaped grooves with an interval of 90°. Mechanically, this configuration can be regarded as an assembly of multiple triangular elements. The mechanical parameters of the force sensor, used in the simulations, are given in Table II. Fig. 4 shows the FEA results under axial and radial forces. Fig. 4 (a) illustrates respectively the strain profiles on the sensor elastomer in the directions of X-, Y-, and Z- axes, and (b) illustrates the corresponding wavelength drifts of the four FBGs. It can be seen that when a load is applied to the sensor in the direction of the Z axis, the strain distributions on all four FBGs are nearly identical. However, in the direction of X- or Y-axis, a pair of FBGs shows a symmetrical response, and the other pair remains virtually unchanged. As a result, the structural design proposed can mitigate cross-sensitivity between the axial and radial forces, but also facilitate the adjustment of sensor stiffness through the parameters change of the dumbbell-shaped grooves.

III. NON-LINEAR DECOUPLING ALGORITHM

A. Conventional decoupling Algorithms

Eq.(7) gives the relationship of the applied force and the wavelength drift of the four FBGs. Inversely, we have

$$\begin{bmatrix} F_x \\ F_y \\ F_z \end{bmatrix} = \gamma \mathbf{S}^{-1} \begin{bmatrix} \Delta_1 \\ \Delta_2 \\ \Delta_3 \\ \Delta_4 \end{bmatrix} \tag{9}$$

where $\mathbf{S}^{-1}$ is the generalized inverse of sensitivity matrix $\mathbf{S}$, and γ is a structural constant.

To establish the above relationship directly, the sensor calibration was done here. During calibration, the wavelength shifts of four FBGs are collected under different known loads, and the transformation matrix is computed by a linear regularized LS fitting algorithm, due to its operation simplicity. This algorithm is highly favored in engineering practice, but its accuracy heavily depends on the quality of the acquired calibration data. Moreover, the fabrication errors of sensor machining and assembly are readily caused, introducing a nonlinear relationship of the applied force and the wavelength shifts. Hence, the model obtained from the linear LS algorithm degrades the accuracy of force calculation.

To improve and decouple multi-axis force computation, a feedforward neural network, namely, BPNN, is studied here. It utilizes backpropagation weight updates as a training mechanism, and can realize nonlinear decoupling. Deliberately, we discuss a BPNN-based decoupling and fault-tolerant model for the force sensor devised. Its topology adopted is 4-400-3. To handle complex wavelength shift data from FBGs, the BPNN model employs the advanced Adam algorithm for parameter iteration and update, and dropout layers and early stopping are applied to mitigate the overfitting risks. In addition, this model utilizes the parameterized rectified linear unit (PReLU) as its activation function, which effectively addresses the issue of negative dead zones.

B. Whale Migration Algorithm Based Kernel Extreme Learning Machine

Kernel extreme learning machine (KELM) is an extended version of traditional extreme learning machine (ELM), which ingeniously addresses the poor robustness of ELM models through kernel function. It implicitly maps data to a high-dimensional kernel function space. During its solution process, the calculation of original hidden layer output matrix is simplified and replaced by a kernel matrix. The KELM topology used here is 4-200-3. To control overfitting, a radial basis function (RBF) kernel is used by incorporating a regularization term. Then, the KELM output function can be given by [30]

$$f(x) = \mathbf{K}(x)^\top \left(\Omega + \frac{I}{C}\right)^{-1} T \tag{10}$$

where Ω denotes the kernel matrix, C is the regularization coefficient, $\mathbf{T}$ represents the training target matrix, and $\mathbf{I}$ is the identity matrix. The kernel mapping vector $\mathbf{K}(x)$ is defined as $\mathbf{K}(x) = [K(x, x_1), K(x, x_2), \ldots, K(x, x_n)]$.

To mitigate the kernel parameter sensitivity and improve the decoupling accuracy of KELM, the Whale migration algorithm (WMA) [31] is utilized for hyperparameter optimization, due to its robust dual-phase search mechanism. It is a bio-inspired metaheuristic optimization method that mimics humpback whales' migration patterns, and can balance global exploration and local exploitation to effectively avoid local optima in high-dimensional search space. The WMA-KELM method, shown in Fig. 5, can achieve nonlinear decoupling of the multi-axis force data.

The KELM algorithm with WMA optimization is implemented through the following steps:

Step 1: First, set the objective function as the RMSE for the cross validation of the leave-one-out method, to enhance

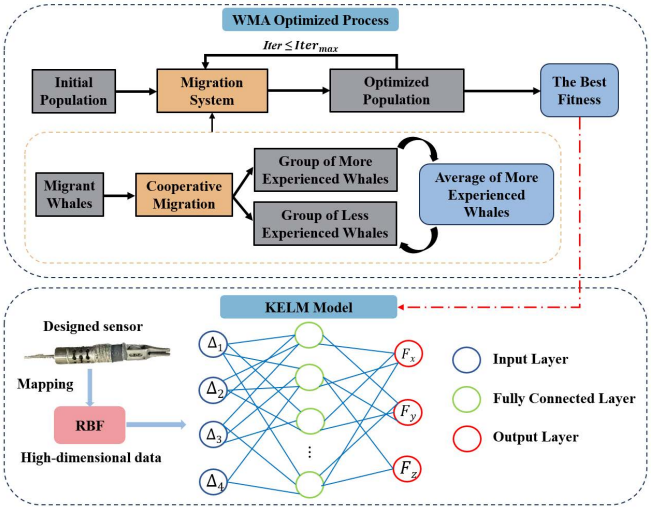

Fig. 5: Nonlinear decoupling with the WMA based KELM algorithm.

the generalization capability of the algorithm. It is given by

$$fitness = \sqrt{\frac{1}{m}\sum_{i=1}^{m}(y_i - \hat{y}_i)^2} \tag{11}$$

Step 2: An initial population of migrant whales is randomly generated between the specified lower bound L and upper bound U, to solve the optimization problem in the searching space with given deterministic parameters.

$$W_i = L + rand(1, D) \odot (U - L), i = 1, 2, \ldots, N_{pop} \tag{12}$$

where $rand(1, D)$ generates the vector of random numbers from the interval $[0, 1]$ in the dimension D, $\odot$ denotes the Hadamard product of two vectors. It produces the elements of a resulting vector by multiplying the corresponding elements of the two original vectors.

Step 3: Within the migrating whale group, the experienced individuals have higher objective function values and responsibility to lead the group to the destination. To describe the actual position of the entire population at any given time,we use the weighted average position (W_{Mean}) of the experienced individuals, yielding

$$W_{Mean} = \frac{1}{N_L}\sum_{j=1}^{N_L} W_j \tag{13}$$

where N_L is the number of the experienced whales, and W_j denotes the position of the jth experienced whale.

Step 4: All the population members are then sorted in descending order in terms of their objective function values, and we have

$$W_1, \ldots, W_{i-1}, W_i, W_{i+1}, \ldots, W_{N_{\text{pop}}} \tag{14}$$

where W_1 is the best member and $W_{N_{pop}}$ is the worst member.

Step 5: W_{Mean} is the current position of the entire migrating whale population. If the distance of W_{Mean} to W_1 is close, it means that the entire population is approaching

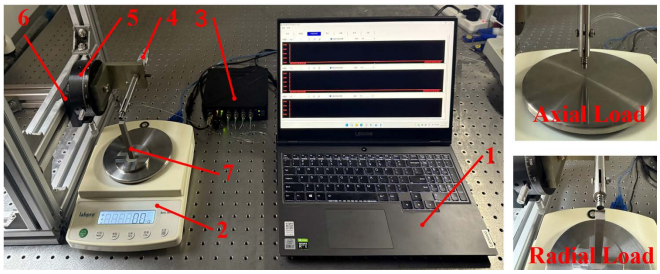

Fig. 6: The calibration platform. 1 laptop, 2 digital electronic scale, 3 interrogator, 4 micrometer, 5 rotation stage, 6 translation stage, 7 radial support.

an optimal value, and the less experienced individuals will move toward the direction $(1, D)$. The new positions of those less experienced individuals are thus computed by

$$\begin{aligned} W_i^{new} = W_{Mean} &+ \text{rand}(1, D) \odot (W_{i-1} - W_i) \\ &+ \text{rand}(1, D) \odot (W_{Best} - W_{Mean}) \\ &i = N_L + 1, \ldots, N_{pop} \end{aligned} \tag{15}$$

and the current position W_i is replaced by the new position W_i^{new} only if $f(W_i^{new}) < f(W_i)$.

Step 6: In the migrating whale group, the more experienced individuals are responsible for selecting the optimal path to the destination. Using the above equation of motion, the ith experienced whale will get the suitable path by

$$\begin{aligned} W_i^{new} = W_i + r_1 \odot L + r_1 \odot r_2 \odot (U - L), \\ i = 1, \ldots, N_L \end{aligned} \tag{16}$$

where r_1 and r_2 are the vectors of random numbers generated from the interval $[0, 1]$, each with dimension of D. L is a position vector, and $(U - L)$ is the relative direction vector. Eventually, the migrating whale population is sorted from best to worst. The topmost N_L members are selected as the leaders of a whale group.

Step 7: When the current iteration number equals the maximum iteration limit, the best member is selected as the optimal solution. If not, the algorithm continues the iteration process.

IV. EXPERIMENTAL RESULTS

A. Force Sensor Calibration

To establish the relationship of the applied forces and the wavelength drift of four FBGs, the devised sensor was calibrated under laboratory conditions. The calibration platform as shown in Fig. 6, comprises of a laptop, a triaxial force sensor, an interrogator (TV-1600-04, Beijing Tongwei Technology Co., Ltd.; 2500 Hz; 1 pm), a digital electronic scale (B15001, Shanghai Liangping Instrument Co., Ltd.; 10 Hz; 0.1 g), a 3DOF platform with micrometer, translation and rotation stages, and a radial support. During the axial (Z-axis) calibration, the sensor tip applies the force perpendicular to the scale, in the range of 0 N to 5 N with an increment of 0.25 N. The wavelength data were acquired simultaneously by the interrogator, while the forces applied

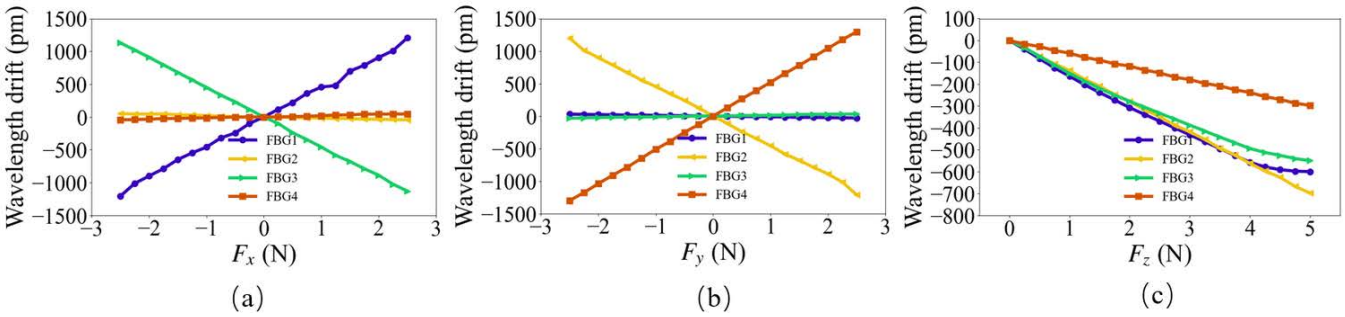

Fig. 7: The calibration results of the sensor under axial and radial forces. (a) F_x, (b) F_y and (c) F_z.

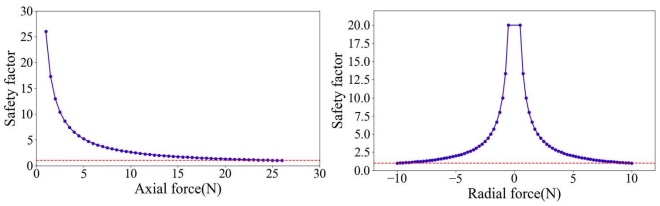

Fig. 8: The safety factor under the axial and radial forces applied.

were recorded from the digital scale. During the radial (X/Y-axis) calibration, the side of the sensor contacts the radial support, and applies forces from -2.5 to 2.5 N with the same increment as the axial direction. Each calibration repeats three times, and the averaged forces and wavelength values are used to reduce noise.

Figure 7 shows the calibration results under axial and radial forces. When the axial force is applied to the devised sensor, the wavelength shift of the four FBGs is basically proportional to the force F_z, as shown in Fig. 7(c). Figs. 7 (a) and (b) show the plots of the wavelength shifts to the axial forces applied. We can see that the results are symmetric and the wavelength shifts of the opposite FBGs are strong correlation with the applied force, while the rest FBGs have no responses nearly. This observation is in agreement with the previous results of FE simulation.

B. Sensor Performance Analysis

The performance of the devised force sensor was evaluated with measurement range, accuracy, and repeatability. Herein, the WMA-KELM model was trained first using the calibration data, and then used to compute the force applied to the sensor from the wavelength shifts of FBGs.

1) Measurement Range: The measurement range is the working load the force sensor can stand without failure or plastic deformation. To ensure sensor safety, the sensor should meet not only the requirement that the working load F_{Work} does not exceed the ultimate load F_{Max}, but also within a margin of safety redundancy. This margin is quantified by the safety factor n, which is defined as

$$n = \frac{F_{Max}}{F_{Work}} \tag{17}$$

The safety factor n represents the operational safety of the sensor within its specified range. $n \geq 1$ is the threshold for a safe sensor. A higher value of n indicates better structural stability. Fig. 8 shows the safety factors of the devised sensor under various axial and radial loads. We can have from this figure that the axial ultimate load is 26 N, and the radial ultimate load 10 N. Hence, the force sensor is within the measurement ranges of the R-LESS system (axial: [0 N,5 N]; radial: [-2.5 N, 2.5 N]). The axial and radial safety factors are over 5.20 and 4.20, respectively. Therefore, the sensor is safe to measure the force within the specified range while maintaining a reasonable margin of structural strength.

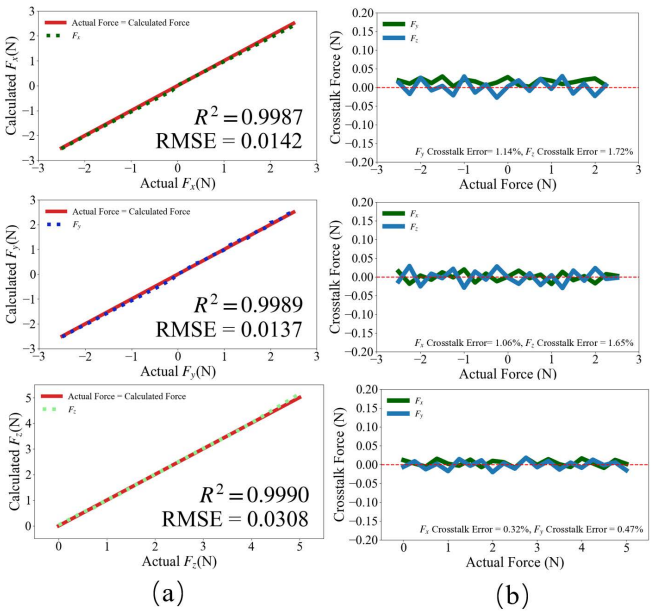

Fig. 9: The sensor accuracy. (a) the calculated vs actual Forces, (b) the crosstalk errors.

2) Accuracy: It reflects the level of uncertainty within the sensor's measurement range. Here, RMSE is used to quantify accuracy. Fig. 9 shows the relationship between the calculated force and the applied force. The slopes of the fitted lines of the triaxial forces are close to 1, with R^2 values of 0.9987 for F_x, 0.9989 for F_y, and 0.9990 for F_z. The corresponding RMSE are 0.0142 N (0.56% FS) in the X axis, 0.0137 N (0.55% FS) in the Y axis, and 0.0308 N (0.62% FS) in the Z axis. Furthermore, it can be seen in Fig. 9 that, when a unidirectional force is applied, the crosstalk errors in the other directions are negligible.

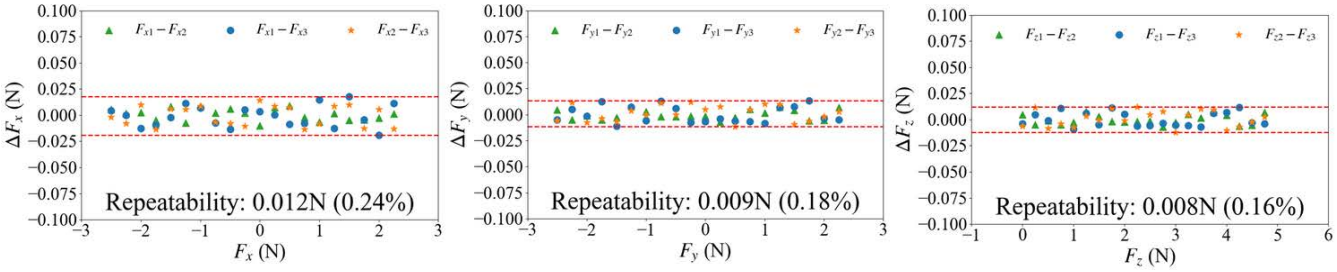

Fig. 10: The repeatability of the devised force sensor in the three different directions.

TABLE III

PERFORMANCE OF DECOUPLED MODELS AFTER INTEGRATION

Algorithm	F_x RMSE (N)	F_y RMSE (N)	F_z RMSE (N)	Predict time (s)
LS	1.324	1.863	1.843	**0.030**
BPNN	0.258	0.473	2.344	0.471
KELM	0.242	0.364	0.537	0.040
WMA-KELM	**0.021**	**0.019**	**0.045**	0.039

3) Repeatability: It is the error of the multiple measurements to same force, and indicates the consistency of the calculated forces, and the reliability of the force sensor. Fig. 10 shows the differences of the predicted forces in three experimental trials, and gives the repeatability errors in the directions of three axes, which are ±0.24% in the X axis, ±0.18% in the Y axis, and ±0.16% in the Z-axis.

C. On-site Tests

This devised sensor is attached to the continuum manipulator end of a single-port surgical robot system (SR-ENS-600, Beijing Shurui Robotics Co., Ltd, China), as shown in Fig. 11, to measure the interactive force at the surgical tool tip. The integration of the sensor with the continuum manipulator gives rise to the mechanical property change of the sensor, and thus it is needed to recalibrate in advance. The calibration process is same as done previously. But here the force applied to the digital scale or the support is implemented by controlling the manipulator of the robot system. With the force sensor re-calibrated, we made a comparison study on the decoupling algorithms discussed in Section III. Table III gives the measurement errors of the forces applied in the direction of the X, Y or Z axis, with the decoupling algorithms of LS, BPNN, KELM and WMA-KELM. It can be seen that the RMSE values of WMA-KELM are 0.021 N (0.84%FS), 0.019 N (0.76%FS), and 0.045 N (0.90%FS) in the X, Y, and Z axes, less than the other three algorithms. Moreover, the time to compute the force with WMA-KELM is less than the other three algorithms. Further, we carried out extensive experiments to mimic surgical scenarios, to validate the reliability of the devised force sensor. As shown in Fig. 12, the single-port surgical robot system is controlled to tap or slide on a tissue phantom with the continuum manipulator. The forces of the three axes, computed by WMA-KELM, are given in Fig. 13.

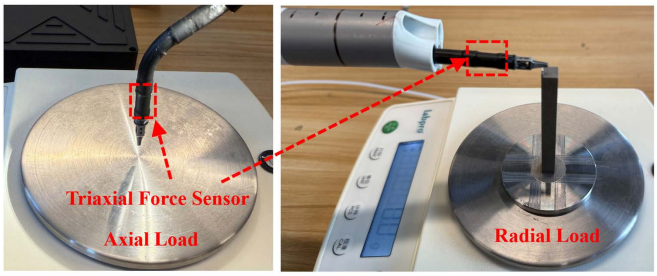

Fig. 11: The force sensor integrated with the continuum manipulator.

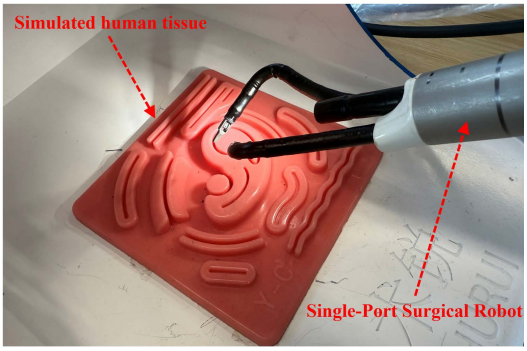

Fig. 12: The force sensor tests on soft tissue phantom.

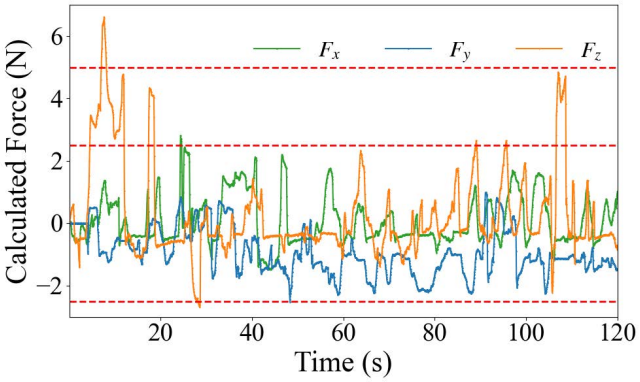

Fig. 13: The applied forces of the three axes to soft tissue phantom, computed by WMA-KELM.

V. CONCLUSIONS

In this paper, a miniature triaxial FBG force sensor is devised with a dumbbell-shaped nickel-titanium alloy structure, and attached to the tool tip of a continuum manipulator of a single-port surgical robot system. The proposed force computation method based on WMA-KELM effectively mitigates nonlinear coupling errors induced by the sensor integration with the continuum manipulator. Experimental results demonstrate that the sensor was successfully integrated into the continuum manipulator, and is able to provide real-time accurate force feedback during on-site tests while maintaining high reliability and stability. Future work will extend to six-axis force sensing and fault-tolerant strategies. In addition, rigorous sensor assessment under clinical environments will be done.

REFERENCES

[1] P. G. Curcillo et al., "Single-port-access (SPATM) cholecystectomy: A multi-institutional report of the first 297 cases," Surgical Endoscopy, vol. 24, no. 8, pp. 1854–1860, 2010.

[2] H. Samson, "Titan medical inc. completes functional prototype of its single port orifice robotic technology (SPORT(TM)) surgical system," Marketwired, Toronto, Canada, 2013.

[3] H. Muaddi et al., "Clinical outcomes of robotic surgery compared to conventional surgical approaches (laparoscopic or open): A systematic overview of reviews," Ann. Surg., vol. 273, no. 3, pp. 467–473, Mar. 2021.

[4] W. Zhang et al., "Research progress and development trend of surgical robot and surgical instrument arm," Int. J. Med. Robot., vol. 17, no. 5, Oct. 2021, Art. no. e2309.

[5] C. H. Kuo, J. S. Dai, and P. Dasgupta, "Kinematic design considerations for minimally invasive surgical robots: an overview," Int. J. Med. Robot. Comput. Assist. Surg., vol. 8, no. 2, pp. 127–145, Jun. 2012.

[6] B. Tang, G. B. Hanna, and A. Cuschieri, "Analysis of errors enacted by surgical trainees during skills training courses," Surgery, vol. 138, no. 1, pp. 14–20, Jul. 2005.

[7] W. Wang, J. Wang, Y. Luo, X. Wang, and H. Song, "A survey on force sensing techniques in robot-assisted minimally invasive surgery," IEEE Trans. Haptics, vol. 16, no. 4, pp. 702–718, Dec. 2023.

[8] L. Yu, Y. Yan, X. Yu, and Y. Xia, "Design and realization of forceps with 3-D force sensing capability for robot-assisted surgical system," IEEE Sensors J., vol. 18, no. 21, pp. 8924–8932, Nov. 2018.

[9] C. Neupert, S. Matich, N. Scherping, M. Kupnik, R. Werthschutzky, and C. Hatzfeld, "Pseudo-Haptic feedback in teleoperation," IEEE Trans. Haptics, vol. 9, no. 3, pp. 397–408, Jul.–Sep. 2016.

[10] A. Abiri et al., "Multi-modal haptic feedback for grip force reduction in robotic surgery," Sci. Rep., vol. 9, no. 1, p. 5016, Mar. 2019.

[11] C. Zhang, J. Guo, B. Chen and S. Zuo, "A Novel 6-DOF Flexible Instrument With High-Resolution Three-Axis Force Sensing Unit for Endoscopic Submucosal Dissection," in IEEE Sensors J., vol. 25, no. 7, pp. 11111-11122, Apr. 2025.

[12] L. Zhang et al., "Force sensing and feedback system based on novel triaxial force capacitive sensor for minimally invasive surgical robot," Adv. Sensor Res., vol. 2, 2023, Art. no. 2300033.

[13] D. O. Uribe, J. Schoukens, and R. Stroop, "Improved tactile resonance sensor for robotic-assisted surgery," Mech. Syst. Signal Process., vol. 99, pp. 600–610, 2018.

[14] A. Song and L. Fu, "Multi-dimensional force sensor for haptic interaction: A review," Virtual Reality Intell. Hardware, vol. 1, no. 2, pp. 121–135, 2019.

[15] D. L. Presti et al., "Fiber Bragg gratings for medical applications and future challenges: A review," IEEE Access, vol. 8, pp. 156863–156888, 2020.

[16] Q. Liang, S. Ouyang, J. Long, L. Zhou, and D. Zhang, "A Novel Fiber Bragg Grating Three-Dimensional Force Sensor for Medical Robotics," IEEE/ASME Trans. Mechatronics, vol. 30, no. 3, pp. 1635-1645, Jun. 2025

[17] A. Gao, Y. Zhou, L. Cao, Z. Wang, and H. Liu, "Fiber Bragg Grating-Based triaxial force sensor with parallel flexure hinges," IEEE Trans. Ind. Electron., vol. 65, no. 10, pp. 8215–8223, Oct. 2018.

[18] Z. Ping, T. Zhang, L. Gong, C. Zhang, and S. Zuo, "Miniature flexible instrument with fibre Bragg grating-based triaxial force sensing for intraoperative gastric endomicroscopy," Ann. Biomed. Eng., vol. 49, no. 9, pp. 2323–2336, Sep. 2021.

[19] T. Li, P. Huang, S. Wang, L. Qiu, C. Li and H. Ren, "Modular and Fault-Tolerant Three-Axial FBG-Based Force Sensing for Transoral Surgical Robots," IEEE Trans. Ind. Electron., vol. 71, no. 12, pp. 16739-16750, Dec. 2024.

[20] L. Gan, J. Wang, L. Xie and Y. Zhou, "A High Precision Triaxial Force Sensor Based on Fiber Bragg Gratings for Catheter Ablation," in IEEE Transactions on Instrumentation and Measurement, vol. 73, pp. 1-11, 2024.

[21] Y. Deng, T. Yang, S. Dai and G. Song, "A Miniature Triaxial Fiber Optic Force Sensor for Flexible Ureteroscopy," IEEE Trans. Biomed. Eng., vol. 68, no. 8, pp. 2339-2347, Aug. 2021.

[22] Y. Deng, L. Hao, T. Yang, S. Dai, and G. Song, "Online Change-Point Detection of Force Signal at the Tip of Surgical Instrument with Morphological Wavelet," in Proc. 27th Int. Conf. Mechatronics and Machine Vision in Practice (M2VIP), Shanghai, China, 2021, pp. 48–53.

[23] S. Li and J. Xu, "Multiaxis Force/Torque Sensor Technologies: Design Principles and Robotic Force Control Applications: A Review," in IEEE Sensors J., vol. 25, no. 3, pp. 4055-4069, Feb. 2025.

[24] T. Li et al., "BP method with rectified linear unit-based nonlinear decoupling for 3-axis FBG force sensor," IEEE Sensors J., vol. 21, no. 3, pp. 2972–2979, Feb. 2021.

[25] H. S. Oh, U. Kim, G. Kang, J. K. Seo, and H. R. Choi, "Multi-axial force/torque sensor calibration method based on deep-learning," IEEE Sensors J., vol. 18, no. 13, pp. 5485–5496, Jul. 2018.

[26] Y. Chen et al., "The SHURUI System: A Modular Continuum Surgical Robotic Platform for Multiport, Hybrid-Port, and Single-Port Procedures," IEEE/ASME Trans. Mechatronics, vol. 27, no. 5, pp. 3186-3197, Oct. 2022

[27] K. Xu, M. Fu and J. Zhao, "Design of the SJTU Unfoldable Robotic System (SURS) for Single Port Laparoscopy," in Proc. 2014 IEEE Int. Conf. Robotics and Biomimetics (ROBIO), Bali, Indonesia, 2014, pp. 53–57.

[28] J. D. Brown, C. E. O'Brien, S. C. Leung, K. R. Dumon, D. I. Lee, and K. J. Kuchenbecker, "Using Contact Forces and Robot Arm Accelerations to Automatically Rate Surgeon Skill at Peg Transfer," IEEE Trans. Biomed. Eng., vol. 64, no. 9, pp. 2263-2275, Sep. 2017.

[29] S. Dargar, C. Brino, K. Matthes, G. Sankaranarayanan and S. De, "Characterization of Force and Torque Interactions During a Simulated Transgastric Appendectomy Procedure," IEEE Trans. Biomed. Eng., vol. 62, no. 3, pp. 890–899, Mar. 2015.

[30] G. B. Huang, H. Zhou, X. Ding, and R. Zhang, "Extreme learning machine for regression and multiclass classification, IEEE Transactions on Systems, Man, and Cybernetics, Part B (Cybernetics), vol. 42, no. 2, pp. 513–529, Apr. 2012.

[31] M. Ghasemi, M. Deriche, P. Trojovský, Z. Mansor, et al., "An efficient bio-inspired algorithm based on humpback whale migration for constrained engineering optimization," Results in Engineering, vol. 25, 2025, Art. no. 104215.